NANO · MICRO
small
www.small-journal.com

Efficient Growth of 1D Van der Waals Heterostructures on Zeolite-Supported SWCNTs

Ruixi Zhang, Dmitry Levshov,* Keigo Otsuka, Ya Feng, Yongjia Zheng, Esko I. Kauppinen, Shohei Chiashi, Wim Wenseleers, Sofie Cambré, Rong Xiang, and Shigeo Maruyama**

The controlled synthesis of 1D van der Waals (1D vdW) heterostructures, specifically single-walled carbon nanotubes encapsulated within boron nitride nanotubes (SWCNT@BNNT), presents a challenge due to an incomplete understanding of the factors influencing BNNT growth. This study investigates the growth yield of SWCNT@BNNT heterostructures produced using zeolite-supported SWCNT templates on SiO_2-coated Transmission Electron Microscopy (TEM) grids, which enable in situ synthesis and thorough evaluation of each step without compromising the nanotube structure. The high-resolution TEM analysis reveals a significant improvement in BNNT coverage on individual nanotubes, increasing from 9% to 42%, through optimization of the ammonia borane precursor amount. A thorough comparison of BNNT growth efficiency is performed using zeolite-supported SWCNT templates against the current benchmark of free-standing SWCNT films, highlighting comparable synthesis yields despite different morphologies and SWCNT diameter distributions. By integrating all Raman and TEM data from the studied SWCNT@BNNT samples, a correlation between BNNT coverage and the intensity of the buckling R-mode of BNNTs is established, providing a reliable criterion for evaluating BNNT growth efficiency in 1D vdW heterostructures. This work advances the understanding and characterization of 1D vdW heterostructures, offering insights into synthesizing hetero-nanotubes using other types of SWCNT templates and paving the way for their diverse applications.

1. Introduction

In recent decades, van der Waals (vdW) heterostructures, created by stacking atomically thin crystals like graphene, hexagonal boron nitride (h-BN), and transition metal dichalcogenides (TMDCs), have emerged as a prominent area of study in the field of materials science.[1–3] The interaction between neighboring layers in these heterostructures results in structural modifications, charge redistribution, and the emergence of intriguing physical phenomena.[2,4,5] Notably, the graphene-hBN 2D heterostructure has sparked significant research interest, delving into topics such as fundamental crystallography, quantum phenomena (such as the Hofstadter butterfly effect, and topological currents), and the development of optical and electronic devices.[2,6–8]

More recently, the exploration of these insightful concepts has been extended to 1D materials.[9,10] A notable achievement in this field was the synthesis of 1D vdW heterostructures by seamlessly wrapping boron nitride nanotubes (BNNT) and molybdenum disulfide nanotubes around single-walled carbon nanotube (SWCNT)

R. Zhang, D. Levshov, K. Otsuka, Y. Feng, Y. Zheng, S. Chiashi, R. Xiang, S. Maruyama
Department of Mechanical Engineering
The University of Tokyo
Tokyo 113–8656, Japan
E-mail: zhangruixi@photon.t.u-tokyo.ac.jp; dmitry.levshov@uantwerpen.be; maruyama@photon.t.u-tokyo.ac.jp

R. Zhang
Department of Bioengineering
The University of Tokyo
Tokyo 113–8656, Japan

The ORCID identification number(s) for the author(s) of this article can be found under https://doi.org/10.1002/smll.202407271

DOI: 10.1002/smll.202407271

D. Levshov, W. Wenseleers, S. Cambré
Department of Physics
University of Antwerp
Antwerp 2610, Belgium

E. I. Kauppinen
Department of Applied Physics
Aalto University School of Science
Espoo FI-00076, Finland

R. Xiang
State Key Laboratory of Fluid Power and Mechatronic Systems
School of Mechanical Engineering
Zhejiang University
Hangzhou 310027, China

R. Zhang
Department of Micro-Nano Mechanical Science and Engineering
Nagoya University
Nagoya 464-8603, Japan

templates.[11] Such a method produced coaxial heteronanotubes that form layer-by-layer structures while preserving the basic morphology of free-standing SWCNT films. This discovery has led to extensive research into the electronic, optical, and thermal properties of 1D vdW heterostructures and related devices.[12–22] For instance, incorporating BNNT as an interfacial layer between channels and gate dielectrics in carbon nanotube transistors improved their performance and helped mitigate threshold voltage variation and hysteresis.[23] However, despite the progress in the 1D vdW heterostructure field, challenges still remain in understanding their synthesis mechanism, improving the growth efficiency, and establishing reliable characterization methods.

In our previous work, we primarily grew 1D vdW heterostructures using free-standing SWCNT films,[24] vertically-aligned SWCNTs,[25] or chirality-sorted SWCNTs[26] as templates. While these templates provided convenient platforms for synthesis, they yielded relatively small amounts of heterostructures, complicating macroscopic ensemble studies and applications. One potential solution to this issue involves using SWCNTs synthesized on zeolite-supported catalysts (referred to as "zeolite-based SWCNTs", as follows), which possess small diameters (0.8–1.2 nm) and can be produced in larger quantities.[27] In our previous study, we used 3D powder-like zeolite-based SWCNT templates to synthesize SWCNT@BNNT heterostructures.[28] However, when attempting to apply the synthesis protocols established for free-standing SWCNT@BNNT films, the final yield of zeolite-based SWCNT@BNNT heteronanotubes was not high, possibly due to differences in growth parameters, accessibility of the BN precursors to the tube surface, or different synthesis mechanisms.

In this work, we therefore present a more systematic study of the BNNT growth process on zeolite-supported SWCNTs, aimed at enhancing BN coverage on this type of SWCNT template. To achieve this, we employ high-temperature-stable and chemically resistant Transmission Electron Microscopy (TEM) grids to support the zeolite particles enabling an in situ high-temperature chemical vapor deposition (CVD) growth and allowing for various structural characterizations at each growth stage without sample processing. By combining high-resolution TEM and Raman mapping, we thoroughly assess the efficiency of BNNT coating and systematically compare the morphology and growth efficiency of zeolite-based samples with current benchmark samples, namely free-standing SWCNT@BNNT films.[29] Notably, we observed a significant increase in the BNNT coverage from 9% to 42% by optimizing the amount of ammonia borane precursor. The developed microscopic characterization method, combining TEM and Raman mapping, proves highly effective for synthesizing 1D heteronanotubes with different types of SWCNT templates and morphologies.

2. Results and Discussion

Figure 1 illustrates the developed approach for the growth of SWCNT@BNNT heterostructures using CVD, as well as the subsequent structural characterization through TEM and Raman spectroscopy. For synthesis (Figure 1a), we utilized SiO_2-coated Mo TEM grids with mesh structures as substrates. These meshes contained over 100 small-sized holes, ≈2–3 µm in diameter, capable of supporting zeolite particles, Fe/Co catalysts, SWCNTs, and hetero-nanotubes (Figure S1, Supporting Information). The SiO_2-coated TEM grids exhibit exceptional thermal stability and can withstand temperatures up to 1100 °C, which allowed us to directly place them in the CVD system for the synthesis of SWCNTs and BNNTs. Additionally, by growing the nanotubes directly on the TEM grid,[27] we eliminated the necessity for post-synthesis transfer, enabling an easy evaluation of each synthesis step (Figure 1a) without compromising the nanotube structure or morphology.

To assess the efficiency of BNNT wrapping around the SWCNTs, we utilized high-resolution TEM directly on the as-synthesized samples, as demonstrated in Figure 1b (note that the high quality and uniformity of the BNNT coating were previously confirmed by electron energy-loss spectroscopy in our earlier studies[11,24] and will not be discussed here). Specifically, we quantified the coverage of the outer BNNTs around isolated SWCNTs using different magnifications, as detailed in Section S2 (Supporting Information). For this statistical assessment, only isolated SWCNTs were considered, as analyzing bundles introduced greater complexity.

Besides TEM, we characterized as-synthesized samples of SWCNTs and SWCNT@BNNTs using Raman spectroscopy. To account for the local sample inhomogeneity, we performed Raman mapping of large areas directly on the TEM grid, as shown in Figure 1c. ≈1000–2500 points were measured for each sample (up to 50 × 50 μm^2 with 1 µm step), both before and after the BNNT growth. The comparison of such SWCNT and SWCNT@BNNT spectra averaged over all the points in the Raman maps are shown in Figure 1d, highlighting all the Raman lines of SWCNT@BNNTs analyzed in this work: radial-breathing mode (RBM), defect-induced D-band and tangential G-band of SWCNTs, and radial buckling R-mode of BNNTs.[30–32] To quantitatively estimate the efficiency of the BNNT coating, we focused on the correlation between the G-band of SWCNTs and the R-mode of BNNTs, as these modes exhibited the simplest behavior. The Raman spectra for these ranges were fitted with a set of Lorentzian functions and subjected to statistical analysis (see Section S4, Supporting Information for details on Raman data processing). Other SWCNT modes, such as the RBM, also exhibited vibrational and electronic shifts following BNNT growth (see Section S5, Supporting Information). However, characterization of their complex behavior requires wavelength-dependent Raman analysis, which is beyond the scope of this manuscript.

It is worth noting that during the analysis, we considered the spectra measured over the substrate and the holes in the TEM grid (points A and B in Figure 1c, respectively) together, as no differences were observed between them (details in Section S1, Supporting Information).

3. Optimizing Growth Efficiency of Zeolite-Based CNT@BNNTs

The growth of BNNTs in the CVD system can be influenced by several factors, including temperature, pressure, synthesis time, precursor type and quantity, and the morphology of the template sample. In this study, to improve the efficiency of BN coating in zeolite-supported SWCNT@BNNTs, we initially explored the impact of the growth time. Our TEM observations revealed that the previously reported 1-h growth conditions (with a fixed precursor

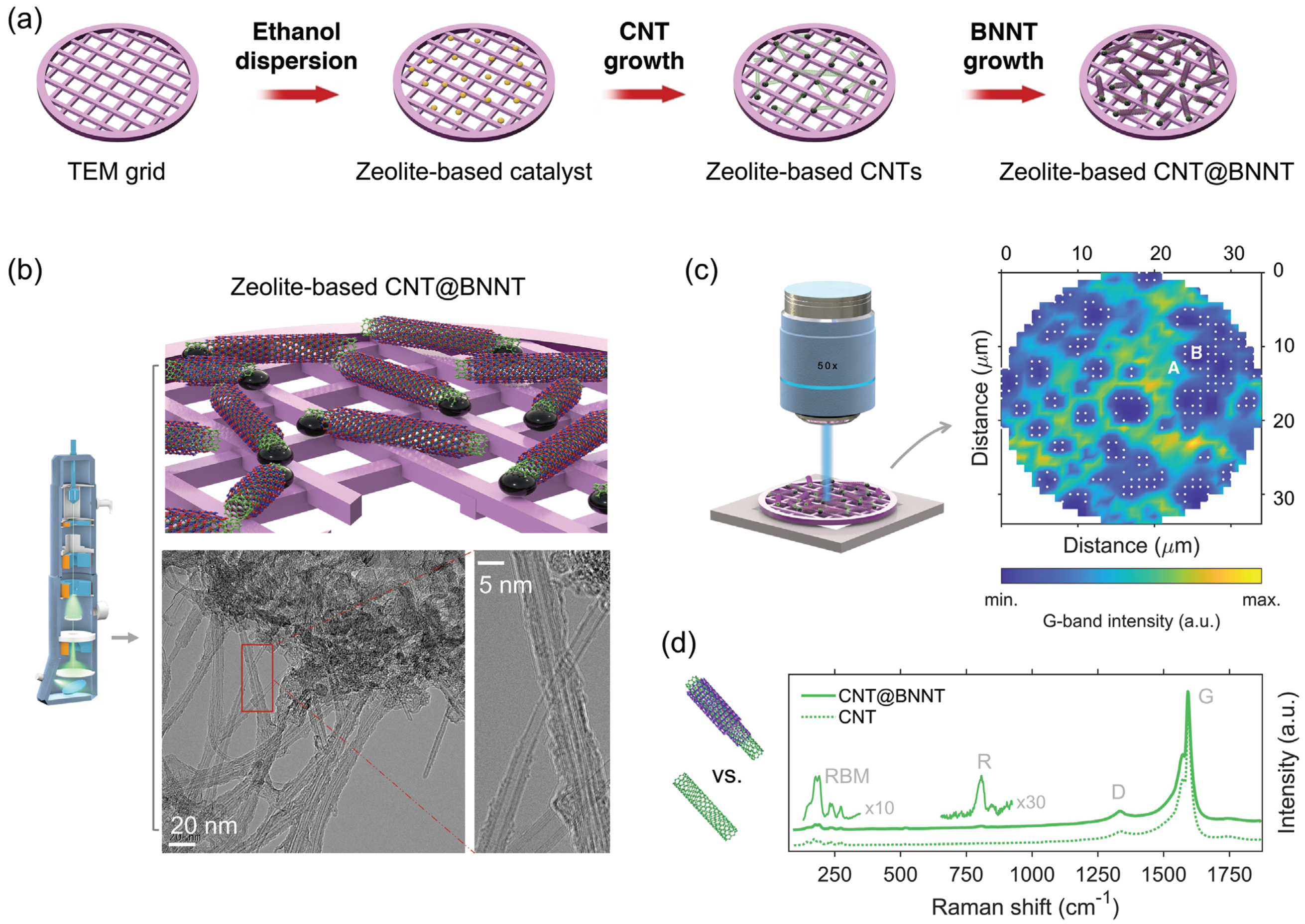

Figure 1. Experimental approach for the synthesis and structural characterization of zeolite-based SWCNT@BNNT heterostructures on SiO_2-coated Mo TEM grids. a) Schematic illustrating the synthesis of zeolite-based hetero nanotubes on the TEM grid. The zeolite-supported catalyst is dispersed in ethanol and drop-casted onto the TEM grid (Figure S1, Supporting Information). CNT and BNNT growth are conducted in different CVD systems. Each synthesis step can be easily evaluated by TEM observation and Raman spectroscopy, as follows. b) High-resolution TEM images for evaluating the growth efficiency on a micro scale, with a focus on determining the coverage of the outer BN shell synthesized on individual SWCNTs. c) Schematic of the Raman mapping process on the TEM grid (left) and the resulting Raman map representing the intensity of the G-band of SWCNTs as a function of the spatial coordinates on the sample surface. d) Comparison of the averaged Raman spectra obtained from the maps measured before and after the BNNT growth.

amount of 50 mg; see Experimental Section)[28] rarely produced BN coating around zeolite-based SWCNTs (Figure S5, Supporting Information), indirectly explaining the absence of clear optical signatures of heterostructures noted in the prior work on zeolite powder.[28] Extending the growth time to 3 h resulted in double-layered BN coatings (Figure S5, Supporting Information), but nearly depleted the supplied amount of ammonia borane precursor (Figure S9a, Supporting Information), highlighting the inefficiency of conventional growth conditions for zeolite-based samples.

Subsequently, increasing the precursor amount from 30 to 90 mg with a fixed growth time of 1 h led to a significant increase in the number of BN layers, as shown in **Figure** 2a. To determine the coverage of BN outer shells under these synthesis conditions, we observed by TEM and statistically analyzed more than 50 randomly selected areas (Figure S6, Supporting Information). We found that synthesis with the 90-mg precursor achieved the best coverage, ≈37%, for the first BN layer, as depicted in Figure 2b. The coverage of the second and third BN layers was also analyzed (represented by blue squares and green triangles in Figure 2b), showing a similar trend to that of the first layer.

We then evaluated the efficiency of the BN coating in the same SWCNT@BNNT samples using Raman mapping. **Figure** 3 displays the radial buckling (R) mode range of averaged Raman spectra for zeolite-supported SWCNT@BNNTs samples, synthesized with different amounts of ammonia borane precursor. They are compared with the reference CNT sample (bottom spectrum) to clearly illustrate the evolution of the R-mode intensity (I_R) of BNNTs. All spectra were normalized by the G-band intensity to account for the variable amount of template SWCNTs under the laser beam. We observed that the R-mode intensity increased with the rise in the amount of the BN precursor, consistent with the trend established in TEM studies in Figure 2b. Specifically, 90 mg led to the highest growth efficiency among all the samples. We also explored the 120 mg growth (top spectrum) but didn't observe any significant improvements compared to the 90 mg case.

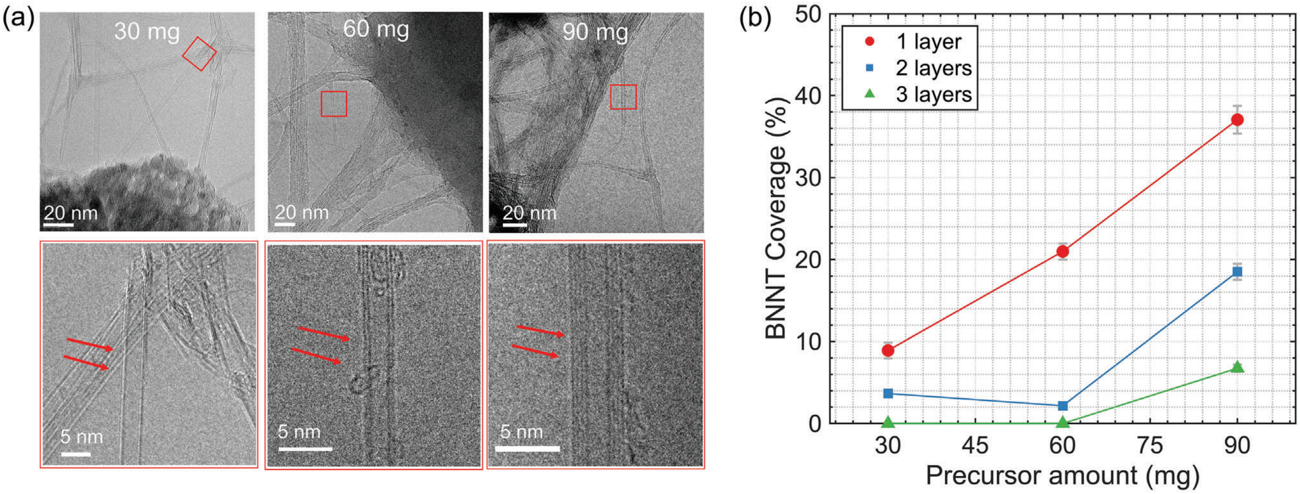

Figure 2. Improvement of the growth of zeolite-based SWCNT@BNNTs. a) Representative TEM images of the zeolite-based SWCNT@BNNTs synthesized with varying amounts of ammonia borane precursor (30, 60, and 90 mg). With an increase in precursor amount, the coverage of the outer BN coating dramatically increased; b) Statistical analysis of BN coverage percentage for zeolite-based SWCNTs (details in Section S2, Supporting Information), showing coverage for one, two, and three BN layers, represented by red circles, blue squares, and green triangles, respectively. For the first BN layer, the coverage percentage increases from 9 to 37% as the precursor amount is increased from the conventional 30 to 90 mg.

To further investigate coating efficiency and reproducibility, we fixed the amount of ammonia borane precursor at 90 mg and prepared additional SWCNT@BNNT samples during different CVD runs, denoted as S1, S2, and S3. Figure 3b–d presents their RBM, R-mode, and G-band spectra before (thin line) and after (thick line) BNNT synthesis, with all spectra normalized to the intensity of the G-band (except in the RBM range, where spectra were normalized to the maximum intensity for clarity). These samples are also compared with the reference CNTs heated at 1075 °C to monitor the effect of high-temperature annealing (dark green lines).

We observed that the RBM lines weakened or even disappeared (Figure S14, Supporting Information), suggesting that some nanotubes were either burned out during BN CVD or their intensities were affected by interlayer coupling, e.g., due to the change in resonance conditions or dielectric screening, as previously observed for double-walled CNTs.[33–35] As for the R-mode intensity, it varied from sample to sample, being strongest for S2 and S3 cases (see also the intensity variation in Figure 3a for 90 mg case). Simultaneously, the G-band frequency[36,37] decreased, reflecting the averaging of Raman responses from numerous different BNNT structures in ensemble samples[29] (dotted curve in Figure 3e), reaching a minimum for the S3 sample at -1.3 cm^{-1}. This variability among S1–S3 samples, despite the consistent precursor amount, may be attributed to the inhomogeneous growth and unstable yield of the CVD process, likely related to the unequal consumption of the precursor (see Figure S9b, Supporting Information and the accompanying discussion). Regarding the effect of high-temperature annealing, it led to the broadening of the G-peak in SWCNT samples and almost no frequency shift (dark green triangle in Figure 3e).

Our TEM studies of the S1–S3 samples confirmed the results of the Raman analysis (Figure 3f). Specifically, the coverage of the first BN layer varied from 32% for S1 to 37% for S2 and finally to 42% for S3. Greater BN coverage was observed in samples with the highest R-mode intensity and a more pronounced G-band redshift.

4. Growth Efficiency of SWCNT@BNNTs With Different Morphologies of SWCNT Templates

We further explored the growth of zeolite-supported hetero-nanotubes by directly comparing them with the current benchmark samples, i.e., the free-standing SWCNT@BNNT films,[29] using the combination of electron microscopy and Raman mapping as presented before. For this purpose and to avoid differences between different CVD runs, the BNNT growth of the film samples was performed simultaneously with the zeolite-based samples in the same CVD system using 90 mg of ammonia borane precursor.

We first compare the morphology of zeolite-based and film samples using SEM and TEM (**Figure 4**), revealing that individual SWCNTs in zeolite-based samples predominantly exist in two distinct states: either distributed across the holes like bridges (illustrated schematically in Figure 4b, top; see also additional TEM images in Figure S10 or SEM images in Figure S16, Supporting Information), or forming 3D dense networks around the zeolite particles, where they intertwine and intersect (Figure 4b, bottom). Examples of grown heterostructures for this sample are shown in the TEM images in Figure 4c. For instance, a single zeolite-based hetero-nanotube is seen stacking over two large bundles (Figure 4c, left), with the BNNT wrapping starting from the edges of the individual carbon nanotubes. Additionally, a fully covered BN shell is displayed, revealing the clear presence of more than four layers of coating (Figure 4c, upper right).

In contrast, the free-standing SWCNT films grown using the aerosol CVD method,[38] exhibit a distinct 2D morphology, where bundles and isolated nanotubes randomly stack on each other, forming a homogeneous structure (Figure 4d,e). After BNNT growth, the free-standing film sample displays a homogeneous

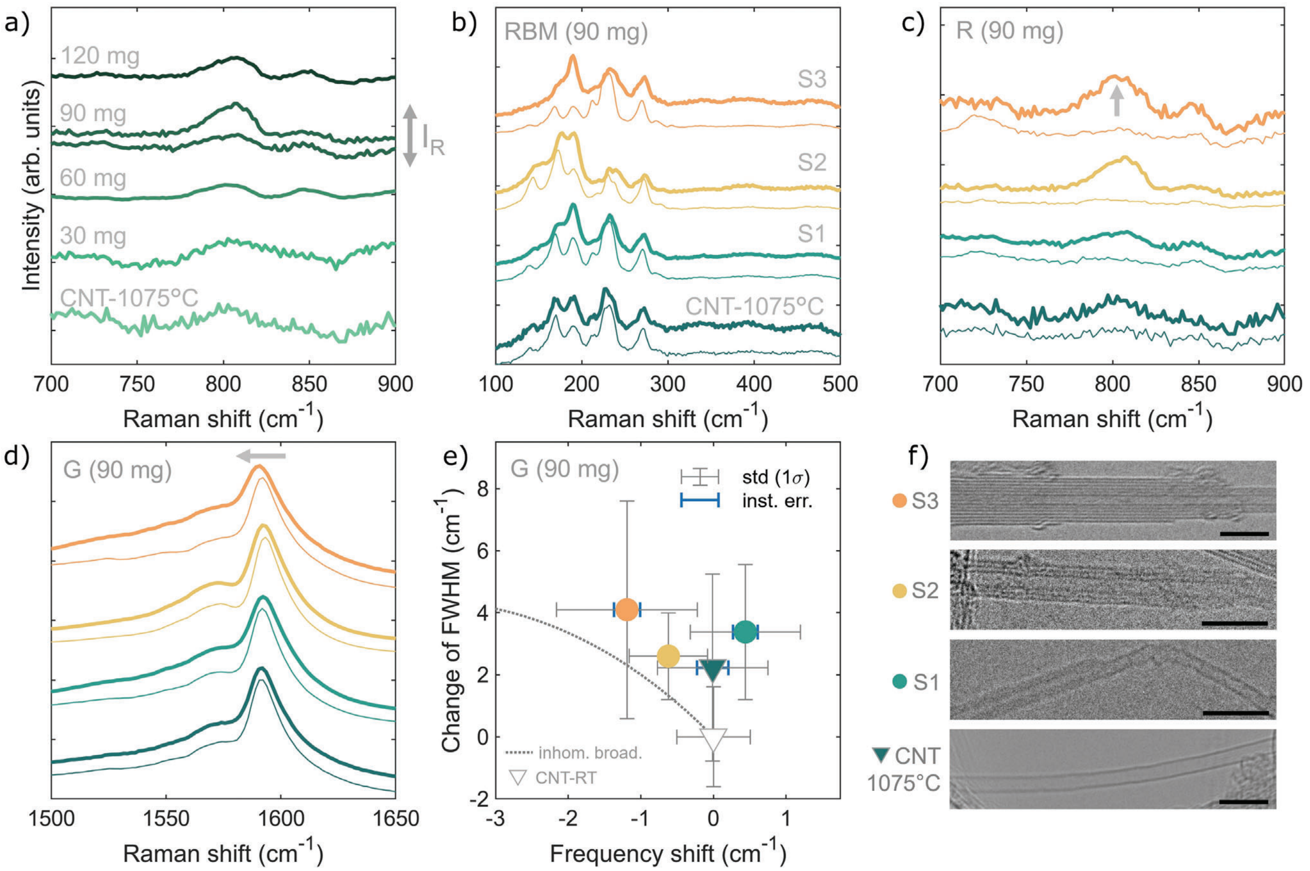

Figure 3. Structural characterization of zeolite-based SWCNT@BNNTs, synthesized via precursor-varying BN CVD. a) Comparison of the R-modes of SWCNT@BNNT heteronanotubes grown with different BN precursor amounts: 30, 60, 90, and 120 mg. The R-mode intensity increases in line with the increase in BNNTs coverage as shown in Figure 2b. b) RBM, c) R-mode, and d) G-band ranges of the averaged Raman spectra of the pristine SWCNT samples (lower thin curves) and resulting SWCNT@BNNT samples (upper thick curves) grown with 90 mg of ammonia borane precursor to check reproducibility. These samples are labeled as S1, S2, and S3 and compared with the reference SWCNT sample annealed at 1075 °C. All spectra in (a–d) were measured at 532 nm. The spectra in (a), (c), and (d) were normalized to the intensity of the corresponding G-band, while those in (b) were normalized to the maximum intensity in the RBM range for clarity. e) Statistical analysis of the G-band in the reference SWCNT (downward green triangle) and SWCNT@BNNT samples (green, yellow, and orange circles for S1, S2, and S3 samples, respectively), highlighting the redshift of the G-band frequency and an increase in full width at half maximum (FWHM) with BN coating. The dotted curve illustrates the effect of G-band frequency downshift and broadening in ensemble samples due to averaging Raman response from a large number of different BNNT structures, as reported in ref. [29] Error bars represent one standard deviation. f) Representative TEM images (from bottom to top) of the reference CNT-1075 °C sample, and S1, S2, and S3 samples of SWCNT@BNNTs. The scale bar corresponds to 5 nm each. Additional images can be found in Figure S10 (Supporting Information).

morphology with a high yield of heterostructures. Figure 4f illustrates more than six individual nanotubes randomly crossing with bundles, each coated by a BNNT shell. Under higher magnification, the BN shells become prominently visible (Figure 4f, right).

To complement the results of the electron microscopy studies, we probed the same samples of the free-standing film and zeolite-based SWCNT@BNNTs by Raman mapping, as illustrated in **Figure** 5a,b, respectively. Additionally, we investigated a macroscopic zeolite-powder sample prepared in accordance with one of our previous works.[28] The microscopic zeolite-based sample on the TEM grid and the macroscopic zeolite-powder samples are labeled Zeol-M and Zeol-P in Figure 5, respectively. We found that in the case of the free-standing films, heteronanotubes displayed a more uniform distribution on the TEM grid, resulting in a consistent G-band signal and a more homogeneous mapping outcome (Figure 5a and demonstrated by the smaller error bars in Figure 5f). On the other hand, it was observed that zeolite-micro samples predominantly grew on the substrate following the distribution of the template SWCNTs and leaving clear empty areas in the middle of the holes (Figure 5b), consistent with the morphology described by SEM and TEM in the previous section. Additionally, zeolite-powder heterostructures were irregularly distributed, as shown in Figure 5c.

Next, we compared the changes in the R-mode and G-band spectra between zeolite-based samples and free-standing films in Figure 5d,e. The thin and thick lines represent the spectra of the template SWCNTs and the SWCNT@BNNTs, respectively. An obvious increase in the R-mode intensity and G-band redshift is observed in both the zeolite-micro and the free-standing film samples. After fitting the full Raman maps (Figure 5f), we found that the free-standing films exhibit larger frequency shifts than

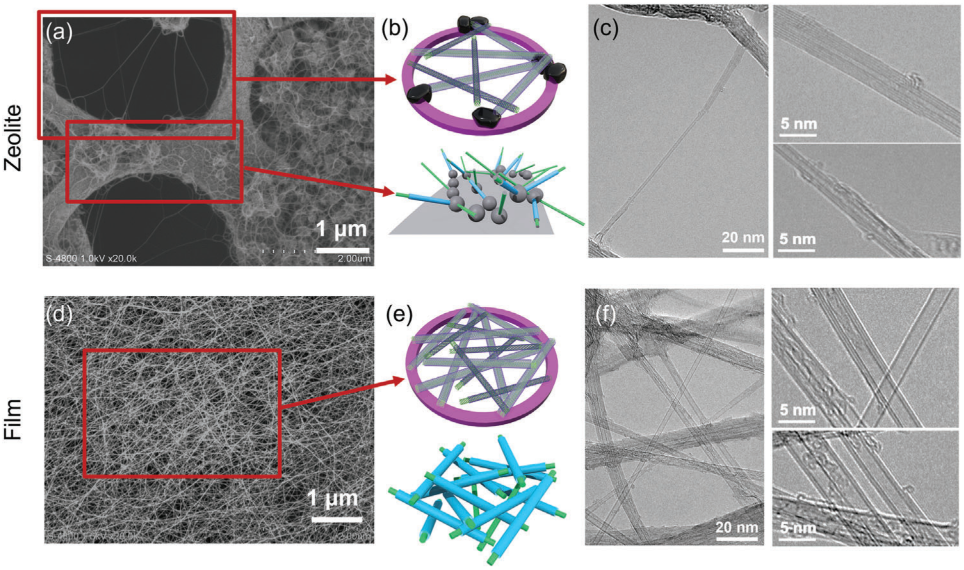

Figure 4. Comparison of SWCNTs and SWCNT@BNNTs grown on the zeolite-based template (top) and on the film template (bottom). SEM images of a) the zeolite-based SWCNT sample and d) free-standing SWCNT films on SiO_2 TEM grid revealing their distinct morphologies. The corresponding schematics of the sample geometry are shown in b) and e), respectively. The TEM images of the SWCNT@BNNTs in c) the zeolite-based sample and f) free-standing film sample. Both samples are grown with 90 mg of ammonia borane precursor (NH_3BH_3).

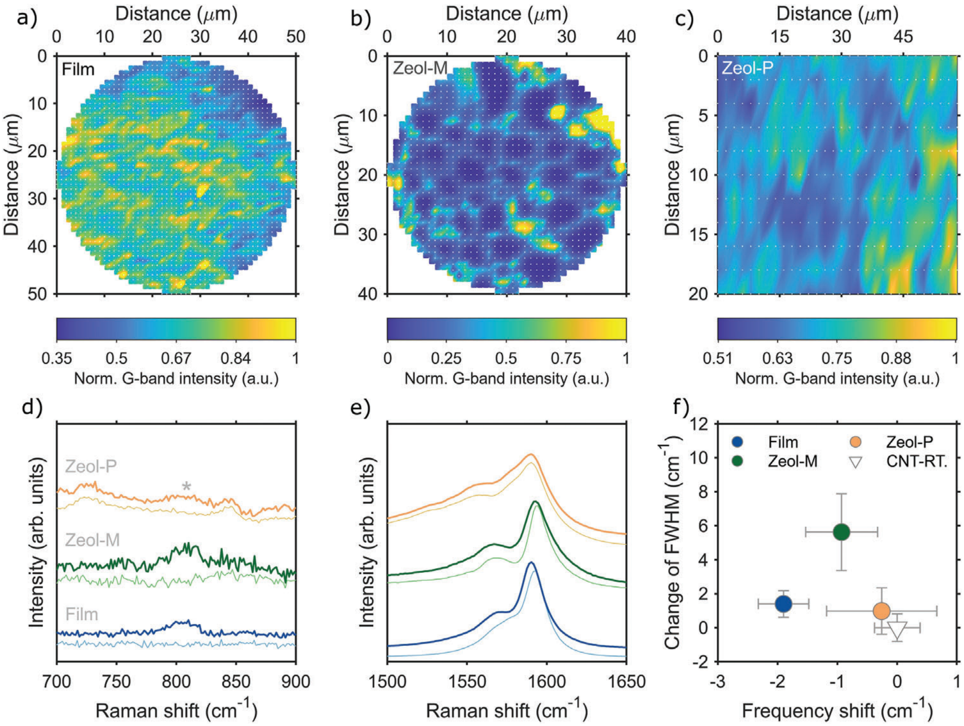

Figure 5. Raman characterization of SWCNT@BNNTs grown on different SWCNT templates: a) free-standing films, b) microscopic zeolite-based sample on the TEM grid (Zeol-M), and c) zeolite-based sample grown on the powder (Zeol-P). The Zeol-P sample shows irregular G-band intensity distribution, Zeol-M sample exhibits G-band signal mainly on the substrate area, while free-standing SWCNT films show a more homogeneous distribution, consistent with SEM observations described in Figure 4. d) R-mode and e) G-band ranges of the average Raman spectra for the free-standing film (blue), Zeol-M (green), and Zeol-P samples (orange). Thin and thick lines represent SWCNT templates and SWCNT@BNNTs, respectively. Zeol-M and film samples were probed at 488 nm, while Zeol-P was probed at 532 nm (note that laser excitation minimally affects the G-band shift, as evidenced in ref. [29]). The star * in (d) indicates the presence of a small R-mode in the Zeol-P sample. f) Scatter plots for the G-band, illustrating the effect of BNNT coating on frequency and FWHM for Zeol-M (green points), free-standing film (blue), and Zeol-P samples (orange). Error bars represent one standard deviation.

zeolite-micro samples under identical growth conditions (−1.8 cm^{-1} vs −0.8 cm^{-1}), indicating better coverage of BNNTs. The greater increase in FWHM observed in the zeolite samples can be explained by the broader diameter distribution of the template SWCNTs compared to the film samples (see comparison of RBM ranges in Figure S14, Supporting Information). This wider distribution results in a greater range of BNNT diameters during CVD growth, which, in turn, leads to a larger increase in G-band linewidth when averaging the Raman response across the entire distribution. Furthermore, the zeolite-micro SWCNT@BNNTs (dark green point) show a higher standard deviation, as indicated by the error bars in Figure 5f, which can be attributed to a smaller quantity of these nanotubes being measured (fewer statistics) due to a large number of holes on the sample surface.

Interestingly, in the case of zeolite-powder samples, both the R-mode intensity and G-band frequency show minimal change during BNNT growth, as indicated by the orange lines in Figure 5d,e. This observation aligns with the absence of clear SWCNT@BNNT spectral signatures reported during earlier studies on zeolite-powder templates.[28] Conversely, for the Zeol-M templates in this study, these spectral signatures are clearly visible (green curves in Figure 5), representing a clear improvement in synthesis efficiency compared to previous research on zeolite templates.

The observed difference in growth efficiency between the film and zeolite-based samples can be tentatively explained by their distinct morphologies and/or different diameter distributions (1.3–2.0 nm for the former vs 0.8–1.2 nm for the latter). For instance, the film samples primarily have a 2D (planar) morphology with numerous easily accessible BNNT nucleation points at the intersections of SWCNTs (Figure 4f).[11,24] In this case, high BNNT coverage can be achieved with relatively short synthesis times, and introducing excessive amounts of ammonia borane precursor does not significantly enhance growth efficiency, as demonstrated in Figure S8 (Supporting Information). In contrast, the zeolite-based samples possess a 3D network of entangled SWCNTs around zeolite particles (Figure S17, Supporting Information), which likely complicates the access of the BN precursor to the nucleation points at the innermost SWCNTs. As a result, these zeolite-supported samples exhibit lower growth efficiency compared to the film samples when supplied with the same amount of BN precursor (Figure 5f). Moreover, the smaller zeolite-based SWCNT templates induce the growth of smaller-diameter BNNTs, which are known to have higher strain energy,[39] making the growth less energetically favorable compared to the larger diameter SWCNTs and BNNTs in the films.

5. Characterization of the Growth Efficiency of SWCNT@BNNTs by Combining Electron Microscopy and Raman Mapping

Finally, we quantitatively combine all the TEM and Raman data obtained from various types of SWCNT@BNNT samples to achieve a more accurate evaluation of BNNT growth efficiency. In addition to the zeolite-based SWCNT@BNNTs and SWCNT@BNNT films discussed earlier, we analyze a set of zeolite-based ^{13}CNT@BNNT heterostructures grown with the SWCNT template highly enriched in the ^{13}C isotope. These samples allow for a better understanding of the quenching of BNNT modes in 1D vdW heterostructures due to interlayer coupling (the synthesis procedure and the Raman analysis of ^{13}CNT@BNNTs will be reported elsewhere).

We fitted the averaged Raman spectra of all samples with a series of Lorentzians and calculated the ratio I_R/I_G of the integrated intensities of the R-mode of BNNTs and the G^+ mode of SWCNTs, as depicted in **Figure 6a** (blue areas). Since pristine SWCNTs exhibit intermediate frequency modes (IFM)[40] in the R-mode range, which can contribute to the total R-mode intensity in SWCNT@BNNTs, we determined the I_{IFM}/I_G ratios for the pristine SWCNT samples. These contributions were then subtracted from the I_R/I_G ratios in SWCNT@BNNT samples to isolate the BNNT signal (note, that without such subtraction the obtained ratios would be excitation energy-dependent due to dispersive character of IFMs). Furthermore, we estimated the BNNT coverage from TEM images by measuring the length of the BNNT coating and the length of the naked SWCNTs (Section S2, Supporting Information), as illustrated in Figure 6b with dashed red and white lines, respectively.

We observed a clear positive correlation between the I_R/I_G ratio and the BNNT coverage estimated by TEM, as shown by the blue dashed line in Figure 6c (the data were fitted using a simple linear model due to the limited experimental range of BNNT coverage). Additionally, we found that the frequency shift of the G-band also correlated with the I_R/I_G and BNNT coverage (Figure S15, Supporting Information). Similar trends were noted in our recent study on SWCNT@BNNT films[29] and were well explained by the effects of interlayer van der Waals interactions.[41–43] However, the quantitative correlation between I_R/I_G and BNNT coverage was not established in that work due to its focus on optical studies rather than TEM. Our current findings definitively establish the I_R/I_G ratio as a reliable criterion for evaluating the growth efficiency of BNNTs in 1D vdW heterostructure samples.

6. Conclusion

This study introduces a systematic method for efficiently growing SWCNT@BNNT heterostructures on a TEM grid using zeolite-based SWCNT templates. Through high-resolution TEM and Raman mapping, we demonstrate a significant enhancement in the growth efficiency of these heterostructures with increasing ammonia borane precursor amounts within the BN CVD system. Optimizing the precursor amount to 90 mg results in a notable improvement in BN coating, increasing the coverage by the first BN layer on individual nanotubes from 9% to 42%.

Additionally, by employing identical BNNT synthesis conditions, we directly compare the growth efficiency using zeolite-based SWCNT templates with the current benchmark, namely free-standing SWCNT films. We find that zeolite-based SWCNT@BNNT samples exhibit slightly lower but still comparable growth efficiency to the film templates, despite differences in template morphology and diameter ranges.

Importantly, by integrating all Raman and TEM data from the studied samples, we establish a positive quantitative correlation between BNNT coverage and the intensity of the R-mode of BNNTs. This correlation serves as a reliable criterion for evaluating

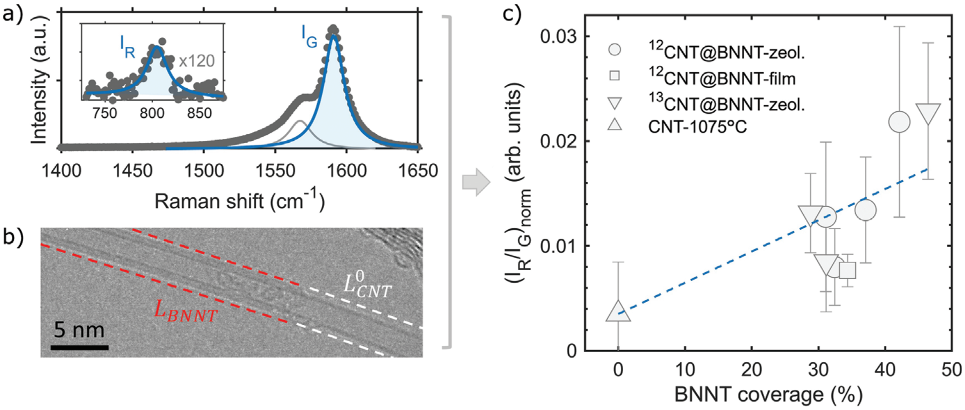

Figure 6. Characterization of BNNT growth by combining TEM and Raman mapping. a) Averaged Raman spectra of SWCNT@BNNTs illustrating the integrated intensity of the R-mode of BNNTs (inset) and the G-mode of SWCNTs used for calculation of the intensity ratio I_R/I_G. b) Representative TEM image for analyzing the coverage of the first BN layer. The lengths of the naked CNT (L^0_{CNT}, white dashed line) and the BNNT (L_{BNNT}, red dashed line) were measured and used to calculate the coverage. c) The correlation between intensity ratio I_R/I_G and BNNT coverage for SWCNT@BNNT samples synthesized using various types of templates: zeolite-based ^{12}CNT@BNNTs (circles), ^{12}CNT@BNNT films (squares), zeolite-based ^{13}CNT@BNNT (downward triangles) compared to the pristine zeolite-based ^{12}CNT sample annealed at 1075 °C (upward triangle). Error bars represent one standard deviation.

the growth efficiency of BNNTs in 1D vdW heterostructure samples. The developed methodology for synthesis and characterization, which combines TEM analysis and Raman mapping, facilitates the exploration of optimal growth parameters and investigation of the intrinsic properties of SWCNT@BNNTs and other carbon nanotube-based vdW heterostructures. Such advancements accelerate the implementation of 1D vdW heterostructures in innovative applications[44] across fields such as nanoelectronics (with SWCNT@BNNTs as conventional FETs,[23] "gate-all-around" FETs[10] or heterojunction diodes[14]), as well as in photonics,[45] and thermal interface materials.[12,46]

7. Experimental Section

Synthesis of SWCNTs: The zeolite-based SWCNT template used in this study was prepared using the alcohol catalytic chemical vapor deposition (ACCVD) method. A Fe–Co catalyst (2.5 wt% for each metal) was employed for SWCNT growth.[27,47] The process involved dissolving 100 ± 5 mg of zeolite-supported co-catalyst powders in 10 mL of ethanol, which was then sonicated for 30 min to ensure proper mixing. The 0.1 mL of the resulting uniform solution was extracted and dispersed onto SiO_2 TEM microgrids, followed by natural drying for 15 min.

Next, the TEM grids were placed in a quartz boat and heated in a quartz tube using an electric furnace. The temperature in the center of the quartz tube was increased to 800 °C, while 300 sccm (standard cubic centimeters per minute) of Ar/H_2 (3% H_2) was simultaneously introduced at a constant pressure of 40 kPa to reduce catalysts. After a 10-min reduction reaction, ethanol vapor was supplied for 5 min, maintaining a pressure of 1.3 kPa in the chamber.

The free-standing SWCNT films used in this work were synthesized using an aerosol CVD method.[38] In this process, ferrocene vapor (floating catalyst) mixed with CO or ethanol (carbon source) was introduced into the high-temperature zone of a ceramic tube reactor. The resulting SWCNTs formed bundles with lengths ranging from 1 to 5 µm and diameters between 1.3 and 2.0 nm. The as-synthesized SWCNT films were directly transferred onto SiO_2 TEM grids for subsequent TEM and Raman characterization.

Synthesis of the BNNTs: The BNNT layers were synthesized by thermal CVD using ammonia borane (NH_3BH_3, 97%, Sigma-Aldrich) as the BN precursor.[11] In short, the zeolite-based SWCNTs on TEM grids were positioned 5 cm downstream from the center of the furnace. The BN precursor was uniformly spread out in the quartz boat, covering an area of 3 ± 0.3 cm^2. It was loaded 40 cm upstream from the furnace center and heated to 70 ± 3 °C using an electric heating belt. The vapor of the BN precursor was then carried by a flow of 300 sccm Ar/H_2 (3% H_2). The temperature inside the reaction chamber was maintained at 1075 ± 5 °C, with a constant pressure of 300 ± 10 Pa.

The BNNT growth conditions previously established for free-standing film samples (referred to as the "conventional growth conditions" in the text)[28] included the use of 30 mg NH_3BH_3 with a growth time of 1 h. To optimize the BN coating, the growth time was varied from 1 to 2 h and then to 3 h, with the amount of NH_3BH_3 fixed at 50 mg. In another run, the growth time was fixed at 1 h but varied the amount of ammonia borane from 30 to 120 mg with a step of 30 mg (the spreading area of the precursor in the quartz boat was roughly controlled to be the same).

Observation of Hetero-Nanotubes by Electron Microscopy: The morphology of both the zeolite-based samples and free-standing films was examined using a Scanning Electron Microscope (SEM) (S-4800, Hitachi Co., Ltd. SEM). The SEM was operated at an acceleration voltage of 1.0 kV and a working distance of 8 mm. To capture high-resolution details, conventional high-resolution TEM (JEM-2800, JEOL) images were taken at an acceleration voltage of 100 kV. The details of the BNNT coverage quantification using HRTEM are presented in Section S2 (Supporting Information).

Raman Spectroscopy Characterization of Hetero-Nanotubes: Raman spectra were acquired using a Renishaw inVia Raman spectrometer equipped with the following laser sources and diffraction gratings: 488 nm (2400 grooves per mm) and 532 nm (1800 grooves per mm). All measurements were performed in a backscattering geometry utilizing a 50x long-distance objective lens (NA = 0.5) in ambient conditions. To prevent potential heating effects on the SWCNTs, the laser power density used during measurements was varied in the range of 10 to 40 kW cm^{-2}. Raman mapping was performed in a point-by-point mode with a scanning area of up to 50 µm × 50 µm with 1 µm steps, including ≈1000–2500 spectra for each sample. To address the calibration uncertainty during the long Raman mapping, reference silicon spectra were consistently measured immediately before and after conducting Raman mapping for each studied sample. The frequency of the Raman spectra in the map was then adjusted by half of the observed shift in the silicon peak (typical absolute shifts were of the order of only 0.25 cm^{-1}). Subsequently, each spectrum with non-zero G-band intensity in the map was fitted by a set of Lorentzian line shapes and the information on the peak position, intensity, and FWHM was collected for subsequent statistical analysis (see details in Section S4, Supporting Information).

Supporting Information

Supporting Information is available from the Wiley Online Library or from the author.

Acknowledgements

R.Z. and D.L. contributed equally to this work. This work was partially supported by JSPS KAKENHI (Grant Numbers JP23H00174, JP23H05443, JP21KK0087) and JST, CREST (Grant Number JPMJCR20B5), Japan. Additional support was provided by a joint JSPS/FWO mobility project (VS0963N), facilitating collaboration between the University of Antwerp and the University of Tokyo. The authors also acknowledge the support from REFEC: Research Foundation for the Electrotechnology of Chubu and NSK Foundation for Advancement of Mechatronics, Japan. TEM part of this work was technically supported by "Advanced Research Infrastructure for Materials and Nanotechnology in Japan(ARIM)" of the MEXT, Japan.

Conflict of Interest

The authors declare no conflict of interest.

Data Availability Statement

The data that support the findings of this study are available from the corresponding author upon reasonable request.

Keywords

boron nitride nanotube, in situ transmission electron microscopy, Raman spectroscopy, van der Waals heterostructure

Received: August 19, 2024
Revised: October 19, 2024

---

[1] A. K. Geim, I. V. Grigorieva, *Nature* **2013**, *499*, 419.
[2] K. S. Novoselov, A. Mishchenko, A. Carvalho, A. H. Castro Neto, *Science* **2016**, *353*, aac9439.
[3] K. Tran, G. Moody, F. Wu, X. Lu, J. Choi, K. Kim, A. Rai, D. A. Sanchez, J. Quan, A. Singh, J. Embley, A. Zepeda, M. Campbell, T. Autry, T. Taniguchi, K. Watanabe, N. Lu, S. K. Banerjee, K. L. Silverman, S. Kim, E. Tutuc, L. Yang, A. H. MacDonald, X. Li, *Nature* **2019**, *567*, 71.
[4] H. Fang, C. Battaglia, C. Carraro, S. Nemsak, B. Ozdol, J. S. Kang, H. A. Bechtel, S. B. Desai, F. Kronast, A. A. Unal, G. Conti, C. Conlon, G. K. Palsson, M. C. Martin, A. M. Minor, C. S. Fadley, E. Yablonovitch, R. Maboudian, A. Javey, *Proc. Natl. Acad. Sci. U S A* **2014**, *111*, 6198.
[5] X. Hong, J. Kim, S. F. Shi, Y. Zhang, C. Jin, Y. Sun, S. Tongay, J. Wu, Y. Zhang, F. Wang, *Nat. Nanotechnol.* **2014**, *9*, 682.
[6] B. Hunt, J. D. Sanchez-Yamagishi, A. F. Young, M. Yankowitz, B. J. LeRoy, K. Watanabe, T. Taniguchi, P. Moon, M. Koshino, P. Jarillo-Herrero, R. C. Ashoori, *Science* **2013**, *340*, 1427.
[7] Y. Liu, N. O. Weiss, X. Duan, H. C. Cheng, Y. Huang, X. Duan, *Nat. Rev. Mater.* **2016**, *1*, 16042.
[8] R. V. Gorbachev, J. C. W. Song, G. L. Yu, A. V. Kretinin, F. Withers, Y. Cao, A. Mishchenko, I. V. Grigorieva, K. S. Novoselov, L. S. Levitov, A. K. Geim, *Science* **2014**, *346*, 448.
[9] S. Cambré, M. Liu, D. Levshov, K. Otsuka, S. Maruyama, R. Xiang, *Small* **2021**, *17*, 2102585.
[10] R. Xiang, S. Maruyama, *Small Sci.* **2021**, *1*, 2000039.
[11] R. Xiang, T. Inoue, Y. Zheng, A. Kumamoto, Y. Qian, Y. Sato, M. Liu, D. Tang, D. Gokhale, J. Guo, K. Hisama, S. Yotsumoto, T. Ogamoto, H. Arai, Y. Kobayashi, H. Zhang, B. Hou, A. Anisimov, M. Maruyama, Y. Miyata, S. Okada, S. Chiashi, Y. Li, J. Kong, E. I. Kauppinen, Y. Ikuhara, K. Suenaga, S. Maruyama, *Science* **2020**, *367*, 537.
[12] P. Wang, Y. Zheng, T. Inoue, R. Xiang, A. Shawky, M. Watanabe, A. Anisimov, E. I. Kauppinen, S. Chiashi, S. Maruyama, *ACS Nano* **2020**, *14*, 4298.
[13] M. Liu, K. Hisama, Y. Zheng, M. Maruyama, S. Seo, A. Anisimov, T. Inoue, E. I. Kauppinen, S. Okada, S. Chiashi, R. Xiang, S. Maruyama, *ACS Nano* **2021**, *15*, 8418.
[14] Y. Feng, H. Li, T. Inoue, S. Chiashi, S. V. Rotkin, R. Xiang, S. Maruyama, *ACS Nano* **2021**, *15*, 5600.
[15] C. Hu, V. Michaud-Rioux, W. Yao, H. Guo, *Nano Lett.* **2019**, *19*, 4146.
[16] P. Ying, J. Zhang, Y. Du, Z. Zhong, *Carbon* **2021**, *176*, 446.
[17] S. Zhao, C. Yang, Z. Zhu, X. Yao, W. Li, *npj Comput. Mater.* **2023**, *9*, 92.
[18] B. Cai, J. Tan, L. Zhang, D. Xu, J. Dong, G. Ouyang, *Phys. Rev. B* **2023**, *108*, 045416.
[19] Y. Nakanishi, S. Furusawa, Y. Sato, T. Tanaka, Y. Yomogida, K. Yanagi, W. Zhang, H. Nakajo, S. Aoki, T. Kato, K. Suenaga, Y. Miyata, *Adv. Mater.* **2023**, *35*, 2306631.
[20] Y. Saida, T. Gauthier, H. Suzuki, S. Ohmura, R. Shikata, Y. Iwasaki, G. Noyama, M. Kishibuchi, Y. Tanaka, W. Yajima, N. Godin, G. Privault, T. Tokunaga, S. Ono, S. Koshihara, K. Tsuruta, Y. Hayashi, R. Bertoni, M. Hada, *Nat. Commun.* **2024**, *15*, 4600.
[21] C. Zhang, J. Fortner, P. Wang, J. A. Fagan, S. Wang, M. Liu, S. Maruyama, Y. Wang, *ACS Nano* **2022**, *16*, 18630.
[22] Y. Yomogida, M. Nagano, Z. Liu, K. Ueji, M.d. A. Rahman, A. Ahad, A. Ihara, H. Nishidome, T. Yagi, Y. Nakanishi, Y. Miyata, K. Yanagi, *Nano Lett.* **2023**, *23*, 10103.
[23] K. Otsuka, T. Sugihara, T. Inoue, W. Jia, S. Matsushita, T. Saito, M. Lee, T. Taniguchi, K. Watanabe, G. Pitner, M. Y. Li, T. A. Chao, R. Xiang, S. Chiashi, S. Maruyama, *Nano Res.* **2023**, *16*, 12840.
[24] Y. Zheng, A. Kumamoto, K. Hisama, K. Otsuka, G. Wickerson, Y. Sato, M. Liu, T. Inoue, S. Chiashi, D. M. Tang, Q. Zhang, A. Anisimov, E. I. Kauppinen, Y. Li, K. Suenaga, Y. Ikuhara, S. Maruyama, R. Xiang, *Proc. Natl. Acad. Sci. USA* **2021**, *118*, 2107295118.
[25] M. Liu, S. Wang, Y. Zheng, M. Takeuchi, T. Inoue, R. Xiang, S. Maruyama, *J. Mater. Res.* **2022**, *37*, 4428.
[26] R. Zhang, Y. Feng, H. Li, A. Kumamoto, S. Wang, Y. Zheng, W. Dai, N. Fang, M. Liu, T. Tanaka, Y. K. Kato, H. Kataura, Y. Ikuhara, S. Maruyama, R. Xiang, *Carbon* **2022**, *199*, 407.
[27] B. Hou, C. Wu, T. Inoue, S. Chiashi, R. Xiang, S. Maruyama, *Carbon* **2017**, *119*, 502.
[28] Y. Feng, H. Li, B. Hou, H. Kataura, T. Inoue, S. Chiashi, R. Xiang, S. Maruyama, *J. Appl. Phys.* **2021**, *129*.
[29] S. Wang, D. I. Levshov, K. Otsuka, B. W. Zhang, Y. Zheng, Y. Feng, M. Liu, E. I. Kauppinen, R. Xiang, S. Chiashi, W. Wenseleers, S. Cambré, S. Maruyama, *ACS Nano* **2024**, *18*, 9917.
[30] R. Arenal, A. C. Ferrari, S. Reich, L. Wirtz, J. Y. Mevellec, S. Lefrant, A. Rubio, A. Loiseau, *Nano Lett.* **2006**, *6*, 1812.
[31] T. Michel, D. Levshov, A. A. Zahab, J. L. Sauvajol, M. Paillet, in *Handbook of Carbon Nanomaterials* (Eds: R. B. Weisman, J. Kono), Vol. *10*, World Scientific Publishing, Singapore **2019**, pp. 75–112.

[32] L. Wirtz, M. Lazzeri, F. Mauri, A. Rubio, *Phys. Rev. B Condens. Matter Mater. Phys.* **2005**, *71*, 2.
[33] G. Gordeev, S. Wasserroth, H. Li, A. Jorio, B. S. Flavel, S. Reich, *Nano Lett.* **2024**, *24*, 8030.
[34] D. I. Levshov, M. V. Avramenko, M. Erkens, H. N. Tran, T. T. Cao, V. C. Nguyen, E. Flahaut, V. N. Popov, A. A. Zahab, J. L. Sauvajol, R. Arenal, W. Wenseleers, S. Cambré, M. Paillet, *Carbon* **2023**, *203*, 801.
[35] Y. Tomio, H. Suzuura, T. Ando, *Phys. Rev. B* **2012**, *85*, 085411.
[36] D. I. Levshov, H. N. Tran, T. Michel, T. T. Cao, V. C. Nguyen, R. Arenal, V. N. Popov, J. L. Sauvajol, A. A. Zahab, M. Paillet, *Phys. Status Solidi B* **2017**, *254*, 1700251.
[37] V. N. Popov, D. I. Levshov, J. L. Sauvajol, M. Paillet, *Phys. Rev. B* **2018**, *97*, 165417.
[38] A. G. Nasibulin, A. Kaskela, K. Mustonen, A. S. Anisimov, V. Ruiz, S. Kivistö, S. Rackauskas, M. Y. Timmermans, M. Pudas, B. Aitchison, M. Kauppinen, D. P. Brown, O. G. Okhotnikov, E. I. Kauppinen, *ACS Nano* **2011**, *5*, 3214.
[39] E. Hernández, C. Goze, P. Bernier, A. Rubio, *Phys. Rev. Lett.* **1998**, *80*, 4502.
[40] A. Vierck, F. Gannott, M. Schweiger, J. Zaumseil, J. Maultzsch, *Carbon* **2017**, *117*, 360.
[41] M. V. Avramenko, M. J. Hokkanen, Y. Slabodyan, M. Ahlskog, D. I. Levshov, *J. Phys. Chem. C* **2022**, *126*, 15759.
[42] S. Rochal, D. Levshov, M. Avramenko, R. Arenal, T. T. Cao, V. C. Nguyen, J. L. Sauvajol, M. Paillet, *Nanoscale* **2019**, *11*, 16092.
[43] M. Erkens, D. Levshov, W. Wenseleers, H. Li, B. S. Flavel, J. A. Fagan, V. N. Popov, M. Avramenko, S. Forel, E. Flahaut, S. Cambré, *ACS Nano* **2022**, *16*, 16038.
[44] R. S. Jones, B. Maciejewska, N. Grobert, *Nanoscale Adv.* **2020**, *2*, 4996.
[45] Z. Zhang, X. Sun, P. Yuan, S. Yokokawa, Y. Zheng, H. Jiang, L. Jin, A. Anisimov, E. Kauppinen, R. Xiang, S. Maruyama, S. Yamashita, S. Y. Set, *J. Lightwave Technol.* **2021**, *39*, 5875.
[46] J. Guo, R. Xiang, T. Cheng, S. Maruyama, Y. Li, *ACS Nanoscience Au* **2022**, *2*, 3.
[47] S. Maruyama, R. Kojima, Y. Miyauchi, S. Chiashi, M. Kohno, *Chem. Phys. Lett.* **2002**, *360*, 229.